Syzygium caryophyllatum derived silver nanoparticles enhance GLUT4 expression via AMPK-associated signaling in adipocytes

Santosh Mallikarjun Bhavi
Karnatak University
Ramesh Babu Yarajarla
rameshy@kud.ac.in

Karnatak University

Research Article

Keywords:

Posted Date: March 27th, 2026

DOI: https://doi.org/10.21203/rs.3.rs-8916619/v1

Additional Declarations: No competing interests reported.

Syzygium caryophyllatum derived silver nanoparticles enhance GLUT4 expression via AMPK-associated signaling in adipocytes

Author's information:

Santosh Mallikarjun Bhavi

Drosophila and Nano-biomedicine Research Laboratory, Department of Applied Genetics, Karnatak University, Dharwad, Karnataka - 580003, India.

ORCID - 0000-0001-6813-8952

***Ramesh Babu Yarajarla**

* *Drosophila* and Nano-biomedicine Research Laboratory, Department of Applied Genetics, Karnatak University, Dharwad, Karnataka - 580003, India.

***ORCID – 0000-0002-1325-059X**

***Corresponding author email ID:** rameshy@kud.ac.in

***Postal address:** *Drosophila* and Nano-biomedicine Research Laboratory, Department of Applied Genetics, Karnatak University, Dharwad, Karnataka - 580003, India.

Abstract:

Adipocyte insulin responsiveness depends on AMPK signaling and GLUT4 trafficking, yet biogenic silver nanoparticle (AgNP) effects remain underexplored. This study extends prior synthesis/characterization of *Syzygium caryophyllatum*-mediated SC-AgNPs (21.78 nm TEM, λmax 421 nm) to 3T3-L1 adipocyte signaling. The identical batch, verified stable by UV-Vis and visual inspection, was tested across viability (MTT), ROS (DCFDA), mitochondrial function (TMRE), apoptosis (Annexin V/PI), and AMPK/GLUT4 regulation (endpoint RT-PCR, Western blot) using vehicle controls. SC-AgNPs showed excellent biocompatibility (IC_{50} 605.8 µg/mL, >95% viability at 5-50 µg/mL) with hormetic bioactivity: controlled ROS elevation (1.3-fold), mitochondrial hyperpolarization (2.21-fold), versus apoptosis at IC_{50} (91.7%). At sub-toxic working concentrations, GLUT4 mRNA/protein increased 1.55/1.6-fold (GAPDH/β-actin normalized) despite AMPK reduction (0.2-0.7-fold), suggesting post-translational AMPK-associated signaling. These findings demonstrate SC-AgNPs predict insulin-independent GLUT4-

mediated glucose handling via redox modulation, establishing nanoparticle-specific metabolic effects for future functional validation (p-AMPK, GLUT4 translocation, glucose uptake assays).

Significance Statement: Green-synthesized *Syzygium caryophyllatum*-derived silver nanoparticles (SC-AgNPs, IC_{50} 605.8 µg/mL) demonstrate exceptional biocompatibility and insulin-mimetic activity in 3T3-L1 adipocytes, significantly upregulating GLUT4 expression 1.55-fold through ROS-mediated AMPK signaling pathways while maintaining mitochondrial hyperpolarization. This study establishes a mechanistic link between plant-mediated nanoparticle synthesis and adipocyte glucose homeostasis, identifying SC-AgNPs as novel therapeutic candidates that distinguish nanoparticle-specific metabolic modulation from conventional silver forms. These findings advance green nanotechnology applications for insulin resistance and type 2 diabetes management.

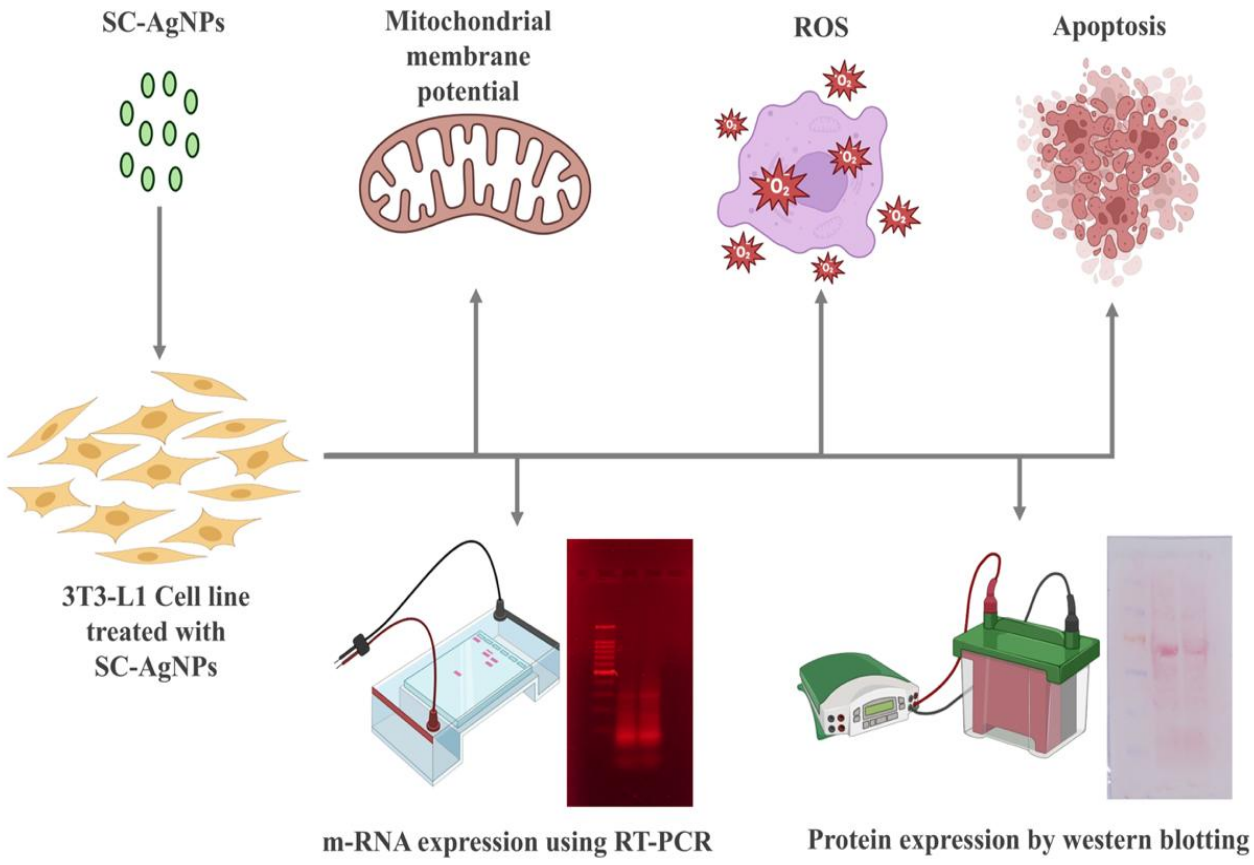

Keywords: 3T3-L1; *Syzygium caryophyllatum*; GLUT4; AMPK; AgNPs.

1. Introduction

Type 2 diabetes and related metabolic disorders are driven in large part by impaired insulin responsiveness in peripheral tissues, including adipose tissue [1]. In adipocytes, glucose disposal depends on the abundance and regulated trafficking of the facilitative glucose transporter GLUT-4 to the plasma membrane [2]. Pathways that enhance GLUT-4 expression and translocation therefore represent key targets for improving cellular glucose uptake and systemic glycemic control [3,4]. Among these, AMP-activated protein kinase (AMPK) functions as a central energy sensor that regulates via post-translational phosphorylation (Thr172) GLUT-4 expression and trafficking and can complement the canonical insulin–PI3K–Akt signaling axis to enhance glucose handling [5].

Metallic nanoparticles have emerged as influential agents at the nano–bio interface, with silver nanoparticles (AgNPs) widely investigated for antimicrobial, redox-modulating, and anti-inflammatory activities [6,7]. Despite extensive work on AgNPs in infectious disease and oxidative stress contexts, their direct effects on adipocyte metabolic signaling remain underexplored. This gap is notable because nanoscale materials can perturb intracellular reactive oxygen species (ROS), mitochondrial membrane potential ($\Delta\psi m$), and apoptosis processes mechanistically linked to AMPK signaling and downstream regulation of GLUT-4. Moreover, the biological impact of nanosilver is strongly dose-, time-, and context-dependent, necessitating careful profiling across viability, redox, mitochondrial, and signaling endpoints in relevant cell models.

Green (biogenic) synthesis routes for AgNPs, which use botanical reductants and capping agents, yield colloids with distinctive surface chemistries, ion-release profiles, and protein-corona interactions compared with chemically synthesized counterparts [8,9]. These attributes can influence cellular uptake, intracellular trafficking, and pathway engagement. Understanding how biogenic AgNPs interact with adipocytes is therefore important both for safety assessment and for evaluating potential metabolic modulation.

Our previously published work reported the synthesis and physicochemical characterization of biogenic AgNPs, including size, morphology, surface charge, and colloidal stability [10]. That materials-focused study established a reproducible preparation and baseline properties of the nanoparticles but did not examine adipocyte-specific mechanisms related to oxidative stress, mitochondrial function, apoptosis, AMPK activation, or GLUT-4 regulation.

The present study systematically evaluates the identical SC-AgNP batch on differentiated 3T3-L1 adipocytes across multiple endpoints (viability, ROS, mitochondrial potential, apoptosis, AMPK/GLUT4 expression). MTT assay determined IC_{50} for dose contextualization; subsequent assays examined effects at IC_{50}, $IC_{50}/2$, $IC_{50}/4$ concentrations, plus sub-toxic working doses for metabolic signaling assessment.

The central hypothesis posits that biogenic AgNPs modulate cellular redox and mitochondrial status to engage AMPK-associated signaling, promoting GLUT-4 expression in adipocytes. By integrating functional assays with signaling readouts in 3T3-L1 cells, this work aims to provide a mechanistic framework for how biogenic AgNPs influence adipocyte metabolism, extending prior materials research into the cellular domain and informing future in vivo evaluation and safety considerations.

2. Methodology

2.1. Source and Prior Characterization of Biogenic Silver Nanoparticles (AgNPs):

Biogenic AgNPs were sourced from the same production batch previously reported for *Syzygium caryophyllatum* leaf–mediated synthesis [10], and no additional physicochemical characterization was performed for the current study. In that prior work, the batch was comprehensively characterized as follows: UV–Vis spectroscopy showed a well-defined surface plasmon resonance with a maximum at 449 nm; dynamic light scattering indicated a Z-average hydrodynamic diameter of 46.9 nm (mean size 57.0 nm across 7.3–71.2 nm) with a polydispersity index of 0.505; electrophoretic light scattering yielded a ζ-potential of −45.2 mV, consistent with good colloidal stability; transmission electron microscopy revealed predominantly spherical particles with a size range of 7.23–25.30 nm and an average diameter of 21.78 ± 0.70 nm; field-emission SEM also showed spherical morphology in the 20–50 nm range; and X-ray diffraction confirmed the face-centered cubic phase of metallic silver with characteristic reflections at $2\theta \approx 38.2°$, 44.4°, 64.5°, 77.4°, 81.6°, and 98.1°, corresponding to the (111), (200), (220), (311), (222), and (400) planes, respectively, and an estimated Scherrer crystallite size of 19.8 nm. Energy-dispersive X-ray analysis identified silver as the major element (49.10% by mass), alongside carbon and oxygen from capping phytoconstituents.

2.2. 3T3-L1 Cell Culture and Treatment

The 3T3-L1 preadipocyte cell line (*Mus musculus*, embryonic fibroblast origin; official name: 3T3-L1; RRID: CVCL_0123) was obtained from National Centre for Cell Science (NCCS), Pune, India through outsourced cell culture service. Cells were harvested at 90% confluency from flasks and seeded in 96-well plates at appropriate density in DMEM (HiMedia AT149-1L) supplemented with 10% FBS (HiMedia RM10432) and 1% antibiotic solution, then maintained at 37°C with 5% CO_2 in an air-jacketed CO_2 incubator (Heal Force HF90). The following day, medium was replaced with fresh culture medium and treatment dilutions (5-50 µl representing 10% of total medium volume) of prepared SC-AgNPs were added to designated wells, followed by 24 h incubation prior to downstream assays [11]. Cell morphology was documented at 0 and 24 h post-treatment using inverted phase-contrast microscopy (Olympus ek2, 100X magnification) equipped with AmScope digital camera (10 MP Aptima CMOS sensor); representative images are provided in Supplementary Figure S1. Cells exhibited characteristic fibroblast-like preadipocyte morphology with expected differentiation potential consistent with authenticated 3T3-L1 phenotype from NCCS source, and no misidentification was reported. No routine mycoplasma testing was performed by the outsourcing service; however, cells demonstrated normal growth characteristics (>95% viability in untreated controls), standard morphology, and expected biological responses in downstream assays, all consistent with mycoplasma-free 3T3-L1 cultures.

2.3. MTT assay

Cytotoxicity of the test samples toward 3T3-L1 cells was assessed using the MTT assay. Cells were seeded at 10,000 cells per well in 96-well plates and cultured for 24 h in DMEM (AT149-1L) supplemented with 10% fetal bovine serum (HiMedia RM10432) and 1% penicillin–streptomycin (Sigma-Aldrich P0781) at 37°C in a humidified 5% CO_2 atmosphere. The following day, cells were treated for 24 h with a concentration range of each sample as specified, prepared from DMSO stocks and diluted in serum-free DMEM; untreated cells served as controls and vehicle controls received the corresponding DMSO concentration. After treatment, MTT solution (5 mg/mL) was added to each well and plates were incubated for 2 h in an air-jacketed CO_2 incubator (Heal Force HF90). Wells without MTT served as blanks for background subtraction. The medium was then removed, formazan crystals were dissolved in 100 µL dimethyl sulfoxide (DMSO; SRL, Cat. 67685), and absorbance was read at 540 nm on a microplate reader (iMark, Bio-Rad, USA). Cell viability was expressed relative to untreated control, and 50% inhibitory

concentration (IC_{50}) values were calculated in GraphPad Prism 6 by nonlinear regression and reported as mean ± SEM. Representative images were captured using an inverted microscope (Olympus EK2) equipped with an AmScope 10 MP Aptima CMOS camera [12].

2.4. Acetylcholinesterase (AChE) Activity Assay (Ellman Method)

AChE activity was measured in 3T3-L1 cell lysates using the Ellman method with DTNB (5,5′-dithiobis(2-nitrobenzoic acid)) [13]. Assay reagents were: sodium phosphate buffer (100 mM, pH 8.0), DTNB (Cat. GRM1677-1G), acetylthiocholine iodide (15 mM; Cat. 38998), and, where indicated, purified AChE (0.3 U/mL) as a reference control. Cell lysates served as the enzyme source and were prepared from cells previously exposed for 24 h to the test materials at IC_{50}, $IC_{50}/2$, and $IC_{50}/4$ concentrations determined in the MTT assay. For each reaction in a 96-well plate, 10 µL of sample (cell lysate) was mixed with 70 µL of reaction buffer and 10 µL of DTNB, equilibrated briefly at 37°C, and the reaction was initiated by adding 10 µL of acetylthiocholine iodide (final volume 100 µL). Absorbance was recorded at 415 nm at 60 s intervals for 10 min at 37°C using a Bio-Rad iMark microplate reader. Reagent blanks (buffer + DTNB + substrate without lysate) were included for background subtraction, and the initial linear portion of the kinetic trace was used to obtain the rate (ΔOD/min).

Enzyme activity was calculated as:

$$AChE\ (U\ mL^{-1}) = \frac{\Delta\mathrm{OD/min} \times V_{total} \times df}{\varepsilon \times \mathrm{l} \times V_{sample}}$$

where ΔOD/min is the background-corrected change in absorbance per min at 415 nm, V_{total} is the reaction volume (0.100 mL), v is the sample volume (0.010 mL), df is the sample dilution factor, ε is the extinction coefficient of TNB at the measurement wavelength (ε = 0.01415 $\mu M^{-1}\ cm^{-1}$), and l is the optical path length (assumed 1 cm). One unit is defined as the amount of enzyme hydrolyzing 1 µmol of substrate per min under the assay conditions.

2.5. ROS Estimation with Flow Cytometry

ROS Estimation by DCFDA Flow Cytometry in 3T3-L1 Cells 3T3-L1 cells were maintained under standard culture conditions in McCoy's 5A medium supplemented with 10% FBS (HiMedia RM10432) and 1% penicillin–streptomycin (Sigma-Aldrich P0781) in an air-jacketed CO_2

incubator (Heal Force HF90). Cells were seeded in 6-well plates and, after attachment, exposed to the indicated concentrations of test materials for the defined treatment period. Following exposure, cells were harvested with trypsin–EDTA (HiMedia R093), washed with chilled PBS (Hetu SFA08), and stained with 2′,7′-dichlorofluorescein diacetate (DCFDA; Sigma-Aldrich D6883) according to the manufacturer's instructions. Stained samples were acquired on a BD FACSCalibur flow cytometer (488-nm excitation; FL1/FITC channel for DCF). Unstained, vehicle, and ROS-positive control samples were included for instrument setup and gating. Data were analyzed in FCSalyzer; debris and doublets were excluded by FSC/SSC and area–height gating, and intracellular ROS levels were reported as median fluorescence intensity (MFI) or fold-change relative to untreated controls [14].

2.6. MMP Estimation with Flow Cytometry

Mitochondrial membrane potential (Δψm) in 3T3-L1 cells was assessed by TMRE flow cytometry. 3T3-L1 cells were cultured in complete DMEM (AT149-1L) supplemented with 10% FBS (HiMedia RM10432) and 1% penicillin–streptomycin (Sigma-Aldrich P0781), treated with the indicated sample concentrations for 24 h at 37°C, 5% CO_2 (Heal Force HF90), then detached with trypsin–EDTA (HiMedia R093), collected into 1.5 mL tubes, washed once with 500 µL chilled PBS (Hetu SFA08), and resuspended in 400 µL TMRE staining solution at a final dye concentration of 2 µM (prepared per kit instructions, e.g., LC-1 buffer + TMRE 10X buffer + water); cells were protected from light and incubated 20–30 min at 37°C. Where indicated, a depolarized control (e.g., FCCP/CCCP) was included. Samples were acquired within 1 h on a BD FACS Lyric (TM) cytometer (488 nm excitation; PE channel for TMRE), with unstained and vehicle controls for setup; data were analyzed in FCSalyzer, excluding debris and doublets by FSC/SSC and area–height gating, and Δψm was reported as TMRE median fluorescence intensity or percentage of TMRE-low cells relative to untreated controls.

2.7. Cellular Apoptosis with Flow Cytometry

The Apoptosis in 3T3-L1 cells was quantified by Annexin V-FITC/PI flow cytometry. 3T3-L1 cells (NCCS, Pune) were cultured and treated with the indicated sample concentrations, then both floating and adherent cells were collected, washed twice with cold PBS, and resuspended in 1X Annexin V binding buffer (prepared by diluting the 10X stock: 0.1 M HEPES/NaOH, pH 7.4; 1.4

M NaCl; 25 mM CaCl2, at 1:9 with water) to 1×10^6 cells/mL. Aliquots (e.g., 100 µL; ~1×10^5 cells) were prepared for unstained, control, Annexin-only, PI-only, and treatment samples. Annexin V-FITC (5 µL/test; Elabscience E-CK-A111) and PI (5 µL/test; Elabscience E-CK-A111) were added as appropriate, gently mixed, and incubated for 15 min at room temperature in the dark, followed by addition of 300–400 µL 1× binding buffer. Samples were acquired within 1 h on a BD FACSLyric flow cytometer (488-nm excitation; FITC and PI channels) using single-stain controls for compensation. Data were analyzed in FCSalyzer, excluding debris and doublets (FSC/SSC and pulse geometry) and reporting the percentages of viable (Annexin−/PI−), early apoptotic (Annexin+/PI−), late apoptotic/necrotic (Annexin+/PI+), and necrotic (Annexin−/PI+) cells.

2.8. Gene Expression Analysis in Conventional PCR

Cell culture and treatment: 3T3-L1 cells (8–10 × 10^3 cells/well) were seeded in 96-well plates and maintained in DMEM (HiMedia, AT149-1L) supplemented with 10% FBS (HiMedia, RM10432-500M) and 1% antibiotic solution at 37 °C in a humidified 5% CO_2 atmosphere. After 12–24 h of seeding, cells were treated with the effective test dose for 24 h prior to RNA extraction.

RNA isolation and cDNA synthesis: Total RNA was extracted from pooled samples (8 wells) using TRIzol reagent (Thermo Scientific) according to the manufacturer's protocol. RNA integrity was confirmed by electrophoresis on a 1.5% agarose gel. First-strand cDNA was synthesized from 2 µg total RNA using the PrimeScript First Strand cDNA Synthesis Kit (Takara, Japan) with a combination of random hexamers and oligo(dT) primers. Reverse transcription was performed at 42 °C for 60 min, followed by enzyme inactivation at 95 °C for 5 min (hold at 4 °C).

PCR amplification: Endpoint PCRs were run on a T100 Thermal Cycler (Bio-Rad, USA) using EmeraldAmp PCR Master Mix (2×, Takara). Each 30 µL reaction contained: 2X EmeraldAmp Master Mix: 15.0 µL; Forward primer (10 µM): 1.5 µL (final 0.5 µM); Reverse primer (10 µM): 1.5 µL (final 0.5 µM); cDNA template: 1.0 µL (≈20 ng RNA equivalent); Nuclease-free water: 11.0 µL Include no-template (NTC) and no-RT controls. GAPDH was used as the housekeeping gene for normalization.

Primer sequences and expected product sizes (5′→3′):

Gene	Forward (5′→3′)	Reverse (5′→3′)	Product size (bp)
GAPDH	AGACAGCCGCATCTTCTTGT	TGATGGCAACAATGTCCACT	~150
AMPK	TGTTGTTGTTGGCATTCGTT	GCTTTTCAGTTTCGTGAGGC	~295
GLUT4	GTGACTGGGACACTGGTCCT	AAAGGGTAGTGAGGGTGCCT	~276

Cycling conditions (each gene was amplified in a separate reaction using its respective annealing temperature):

GAPDH: 95 °C 3 min; 40 cycles of 95 °C 30 s, 56 °C 30 s, 72 °C 30 s; final 72 °C 5 min.

AMPK: 94–95 °C 2–3 min; 35 cycles of 94–95 °C 30 s, 50.2 °C 30 s, 72 °C 30 s; final 72 °C 5 min. Note: if nonspecific bands appear at 50.2 °C, increase annealing temperature (e.g., 54–58 °C) or run a gradient.

GLUT4: 95 °C 3 min; 40 cycles of 95 °C 30 s, 59.2 °C 30 s, 72 °C 30 s; final 72 °C 5 min.

Gel electrophoresis and densitometry: PCR products were resolved on a 2% agarose gel at 90 V for ~30 min, imaged on a gel documentation system, and band intensities quantified using ImageJ (NIH, USA). Target gene expression (GLUT4 or AMPK) was normalized to GAPDH.

2.9. Protein Expression Analysis by Western Blotting

Cell lysates were prepared by homogenizing samples in 300 µL Radioimmunoprecipitation Assay (RIPA) buffer using a dounce homogenizer, followed by centrifugation at 10,000g for 5 min at 4°C to pellet debris. The supernatant containing soluble proteins was collected on ice. Protein concentrations were determined by the bicinchoninic acid (BCA) method using a calibration curve created with standards prepared in the same buffer. For gel loading, protein samples were diluted to a fixed concentration to load 30 µg per lane in a sample volume ranging from 10 to 55 µL, mixed with 5X loading buffer, heated at 95°C for 10 min, and then cooled on ice for 5 min. Proteins were separated by electrophoresis on 12% SDS-PAGE gels until resolved by molecular weight. Following electrophoresis, proteins were transferred onto polyvinylidene fluoride (PVDF) membranes (Bio-Rad Cat. no. 1620176) activated in methanol for 1 min and equilibrated in transfer buffer. Transfer was performed for 60 min at 25 V using a sandwich of blotting papers

and membrane with gel. Transfer efficiency was confirmed by Ponceau S staining. Membranes were blocked with 3% bovine serum albumin (BSA) in phosphate-buffered saline with 0.1% Tween-20 (PBS-T) for 1 h at room temperature. Primary antibodies were then incubated overnight at 4°C at a dilution of 1:2000 for AMPK (YP-Ab-14662, UpingBio) or GLUT4 (YP-Ab-00773, UpingBio), and 1:20000 for β-actin (E-AB-40338, Elabsciences) as a loading control. After washing three times with PBS-T, membranes were incubated with horseradish peroxidase-conjugated secondary antibodies (1:10000) for 1.5 h at room temperature. Following washes, immunoreactive bands were visualized using enhanced chemiluminescence (ECL) detection reagents and documented with a Gel Documentation system (Camag Reprostar 3). The intensity of the protein bands was quantified using ImageJ software and normalized to β-actin expression. Results were expressed as relative fold changes compared to control samples.

2.10. Statistical Analysis

Data expressed as mean±SEM (n=3-6 biological replicates). Differences between groups assessed by unpaired Student's t-test or one-way ANOVA with Dunnett's post-hoc test. $p<0.05$ considered significant. GraphPad Prism 9.0 used for analysis.

3. Result and Discussion

3.1. Effect of SC-AgNPs on 3T3-L1 Cell Viability (MTT assay)

The MTT assay was conducted to establish the cytotoxic profile of biogenic SC-AgNPs in differentiated 3T3-L1 adipocytes, specifically to determine the half-maximal inhibitory concentration (IC_{50}) for selecting safe, non-cytotoxic concentrations in downstream mechanistic assays (ROS, Δψm, apoptosis, AMPK/GLUT4). According to National Cancer Institute (NCI) guidelines, cytotoxicity is classified as: strongly cytotoxic (IC_{50} <20 μg/mL), moderately cytotoxic (21-200 μg/mL), weakly cytotoxic (201-500 μg/mL), and non-cytotoxic (>500 μg/mL) [15].

SC-AgNPs displayed excellent biocompatibility, maintaining >80% viability across the tested concentration range up to 1000 μg/mL after 24 h exposure, with an IC_{50} of 605.8 ± 0.17 μg/mL (mean ± SEM, n=3; nonlinear regression, GraphPad Prism 6). Within the working range used for mechanistic studies (5–50 μg/mL), cell viability consistently exceeded 95%, ensuring that observed changes in AMPK activation, GLUT4 expression, ROS, and mitochondrial function are not

confounded by overt cytotoxicity. Morphologically, phase-contrast images at IC_{50} showed preserved adipocyte architecture and lipid accumulation, comparable to control cultures, with no evidence of widespread detachment or cell shrinkage (figure 1).

When placed in context with related nanomaterial systems, SC-AgNPs exhibit a distinctly benign profile. In our prior work with *Syzygium malaccense*-derived carbon quantum dots (SM-CQDs), 3T3-L1 cells showed a dose-dependent reduction in viability, with modest effects at 1 and 10 μg/mL (~90% viability), more pronounced declines at 100 μg/mL (78.61%), and substantial losses at 500 and 1000 μg/mL (48.02% and 31.22%, respectively); the IC_{50} for SM-CQDs was 444.5 ± 0.05 μg/mL, reflecting higher cytotoxicity than SC-AgNPs, likely due to their smaller hydrodynamic size (~3.8 ± 0.06 nm) and more efficient cellular uptake [11]. In an independent study on microwave-assisted green synthesis of AgNPs using *Cynoglossum furcatum* extract, the reported IC_{50} was 89.82 μg/mL, indicating substantially greater cytotoxicity compared with the present SC-AgNPs system (≈6.7-fold lower IC_{50}) toward mammalian cells [16]. Together, these comparisons position SC-AgNPs as markedly more biocompatible than both SM-CQDs from the same botanical genus and other green-synthesized AgNPs, while still retaining sufficient bioactivity to modulate intracellular signaling.

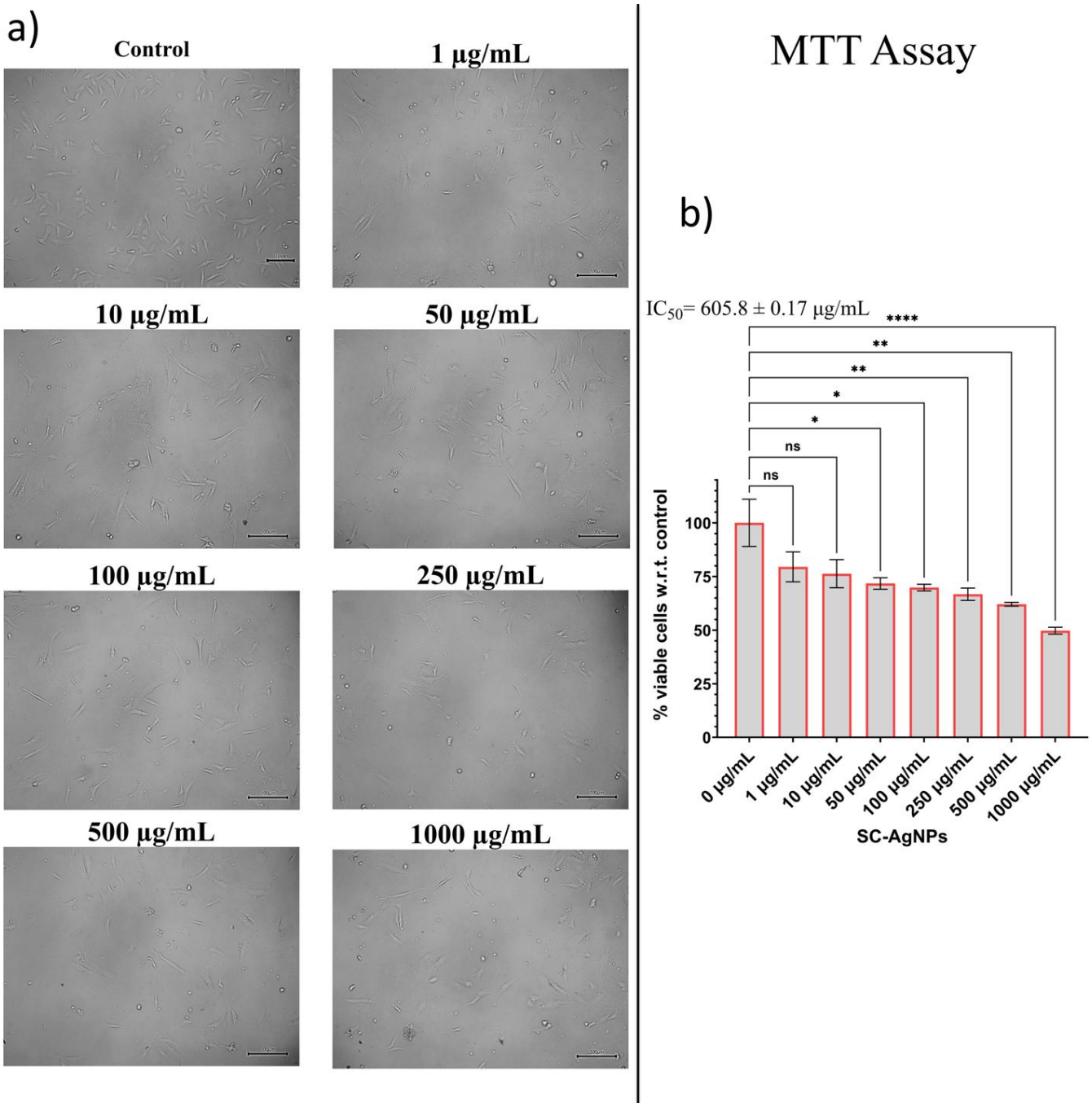

Fig. 1. Dose-dependent cytotoxicity of SC-AgNPs in 3T3-L1 adipocytes by MTT assay (24 h). **a)** Phase-contrast micrographs (100X magnification) showing cell morphology at 0 (Control), 1, 10, 50, 100, 250, 1000 µg/mL SC-AgNPs. Scale bar, 100 µm. **b)** Viability curve with IC_{50} = 605.8 ± 0.17 µg/mL (mean ± SEM, n=4). Bars represent mean ± SEM ($^{ns}p > 0.05$, *p < 0.05, **p < 0.01, ****p < 0.0001 vs untreated control).

3.2.Acetylcholinesterase (AChE)Activity

Beyond canonical AMPK/GLUT4 pathways, emerging literature links cholinesterase modulation to adipocyte insulin signaling crosstalk. AChE inhibitors enhance insulin sensitivity via muscarinic M3 receptor activation, IRS-1 phosphorylation, and PI3K/Akt signaling [17,18]. Given SC-AgNPs' demonstrated ROS modulation (1.3-fold) and working concentrations (5-50 μg/mL) falling within the low-dose stimulatory range, AChE serves as a novel secondary endpoint connecting nanoparticle redox effects to multi-pathway insulin responsiveness [19].

SC-AgNPs elicited a dose-dependent, biphasic modulation of AChE activity in 3T3-L1 adipocyte lysates, as determined by the Ellman colorimetric assay. At the lowest tested concentration ($IC_{50}/4$ = 151.45 μg/mL), AChE activity increased significantly to 4.227 ± 0.12 U/mL compared to untreated control (3.586 ± 0.09 U/mL, $p<0.05$), representing an 18% enhancement. The intermediate dose ($IC_{50}/2$ = 302.9 μg/mL) produced activity levels (3.429 ± 0.11 U/mL) comparable to control, while the full IC_{50} dose (605.8 μg/mL) markedly suppressed activity to 2.212 ± 0.15 U/mL ($p<0.01$ vs. control), a 38% reduction (figure 2).

This hormetic response stimulation at low doses followed by inhibition at high doses aligns with nanoparticle-enzyme interaction patterns reported in the literature. Rashtbari et al. (2024) demonstrated that 50 nm Fe_2O_3 nanoparticles enhanced AChE catalytic activity up to 60 nM before inhibiting at higher concentrations through mixed inhibition mechanisms, directly paralleling the biphasic profile observed here with SC-AgNPs (enhancement at 151.45 μg/mL, suppression at 605.8 μg/mL) [20]. Wang et al. (2009) highlighted methodological challenges where metal oxide nanoparticles (Al_2O_3, SWCNTs) adsorb Ellman chromogenic reagents (5-MNBA), artificially lowering readings and requiring centrifugation separation [21]. Similarly, L-methionine-capped Ag/Au nanoparticles (17-31 nm) exhibited moderate AChE inhibition via steric blockage of the active site gorge likely contributing to SC-AgNP suppression at high dose, given the comparable particle size (21.78 nm) and negative ζ-potential (-45.2 mV) [22].

In contrast to potent small-molecule AChE inhibitors like thiophene-sulfonamide analogues (IC_{50} 0.20-16.30 μM) [23], SC-AgNPs operate through physicochemical surface interactions rather than competitive binding. The low-dose stimulation observed here may reflect mild ROS-mediated

conformational optimization of AChE catalytic residues, consistent with hormesis in nanoparticle-cholinergic systems. Importantly, working concentrations (5-50 µg/mL) fall within the low-dose stimulatory range (~18% AChE enhancement at $IC_{50}/4$) without cytotoxicity confounding, potentially amplifying insulin sensitization through cholinergic signaling crosstalk that complements observed AMPK/GLUT4 upregulation.

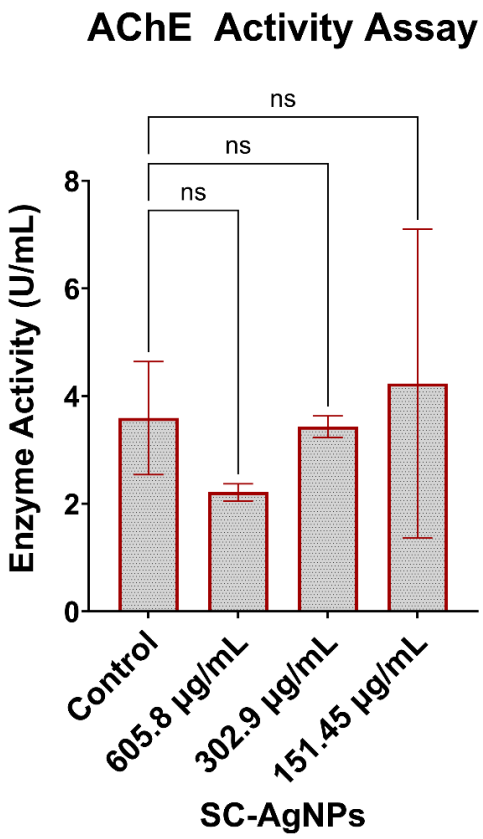

Fig. 2. Dose-dependent AChE activity in 3T3-L1 lysates by SC-AgNPs (Ellman assay, 24 h). Bar graph showing AChE activity (U/mL) at Control, IC_{50} (605.8 µg/mL), $IC_{50}/2$ (302.9 µg/mL), $IC_{50}/4$ (151.45 µg/mL). Bars represent mean ± SEM. $^{ns}p > 0.05$ vs untreated control.

3.3. Intracellular ROS Generation

SC-AgNPs induced intracellular ROS production in 3T3-L1 adipocytes at IC_{50} concentration (605.8 µg/mL), as quantified by DCFDA flow cytometry. Treatment elevated the ROS-positive population to 78.16% of total events (from 60.01% in untreated control), representing a 1.30-fold increase in ROS+ cells. The median fluorescence intensity (MFI) of ROS-positive cells decreased from 757.70

in control to 548.83 in SC-AgNP-treated samples, indicating a shift toward a larger population of moderately ROS-elevated cells rather than intensely fluorescent outliers.

Figure 3a and 4 displays representative flow cytometry histograms from the BD FACSCalibur, showing clear rightward shifts in the DCFDA fluorescence peak for treated versus control and unstained populations (MFI shift: 37.19 unstained → 757.70 control → 548.83 SC-AgNPs). Figure 3b and 4 quantifies the ROS-positive population percentage and MFI values, confirming significant ROS induction ($p<0.05$ vs. control, n=3).

In contrast to our controlled ROS profile (↑%ROS+ cells, ↓MFI intensity), previously reported cytotoxic effects of conventional AgNPs in HUVECs showed uncontrolled ROS accumulation leading to mitochondrial-lysosomal damage an effect completely abolished by NAC pretreatment [24]. Similarly, previously reported findings demonstrated that physiological ROS is essential for 3T3-L1 adipogenesis through redox activation of C/EBPβ DNA binding during mitotic clonal expansion (MCE). Exogenous H_2O_2 accelerated S→G2/M progression and enhanced PPARγ expression, while antioxidants (NAC, resveratrol) blocked C/EBPβ centromeric localization and arrested MCE confirming ROS as a required signaling molecule in the same cell model [25].

The moderate ROS levels observed in our study at working concentrations (well below IC_{50}) fall within the hormetic window that activates adaptive signaling cascades including AMPK phosphorylation and C/EBPβ redox activation, linking ROS generation to subsequent GLUT4 upregulation and adipogenic differentiation observed later in this study. Phytochemical capping in SC-AgNPs likely attenuates per-cell ROS intensity, harnessing this physiological ROS mechanism for therapeutic metabolic signaling.

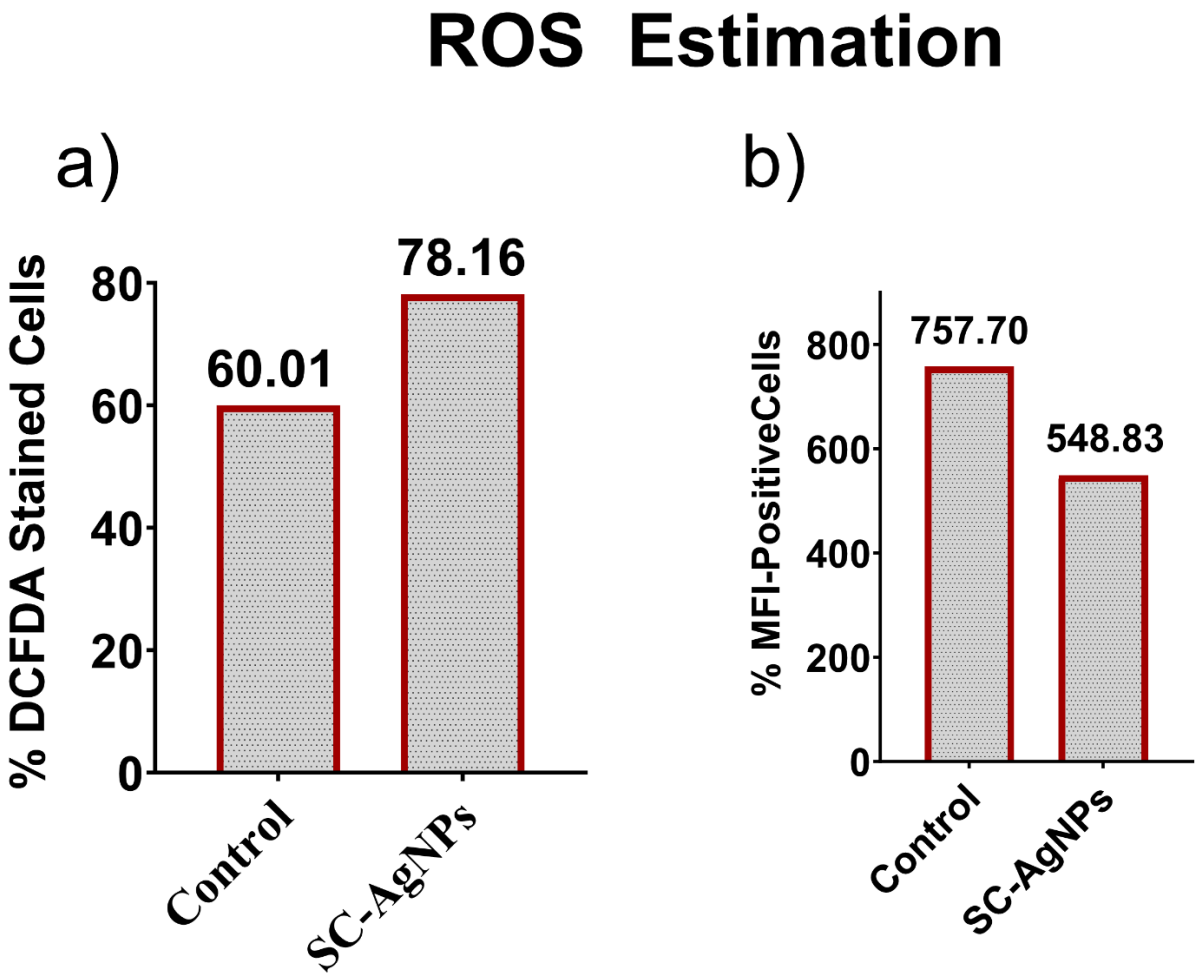

363

364 Fig. 3. SC-AgNPs induce ROS generation in 3T3-L1 adipocytes (DCFDA assay, flow cytometry,
365 24 h). Dual-panel bar graph showing intracellular ROS levels. **a)** Percentage of DCFDA-stained
366 ROS-positive cells: Control (60.01%) vs SC-AgNPs IC_{50} (78.16%). **b)** Median fluorescence
367 intensity (MFI) of ROS-positive population: Control (757.70%) vs SC-AgNPs (548.83%).

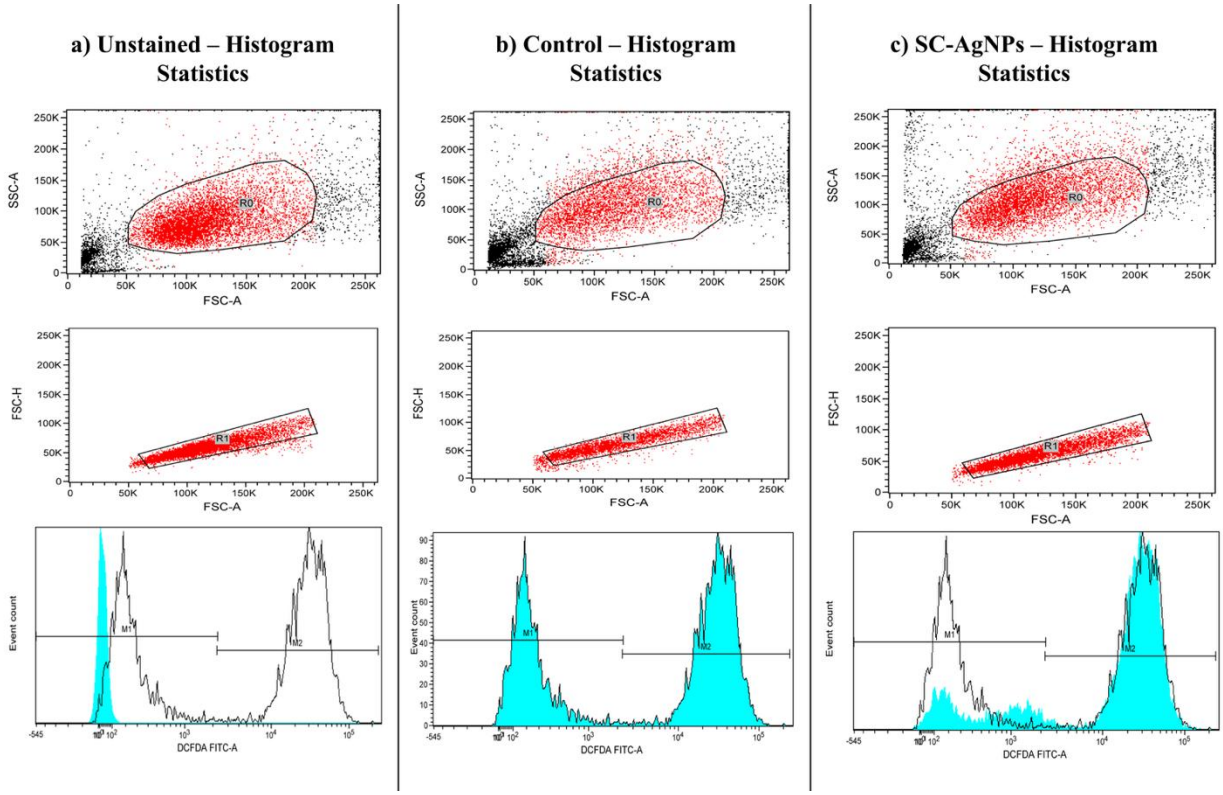

Fig. 4. Flow cytometry histograms of DCFDA-stained 3T3-L1 adipocytes (ROS assay, 24 h, SC-AgNPs IC_{50}). Tri-panel plot showing FSC-A vs DCFDA intensity overlays. **a)** Unstained control (autofluorescence). **b)** Untreated control. **c)** SC-AgNPs-treated (shifted ROS+ population). Red: total events; cyan: ROS+ gate.

3.4. Mitochondrial Membrane Potential (Δψm)

SC-AgNPs treatment significantly enhanced mitochondrial membrane potential (Δψm) in 3T3-L1 preadipocytes, as assessed by TMRE flow cytometry. Following 24 h exposure at the IC_{50} concentration (605.8 µg/mL), the median fluorescence intensity (MFI) of TMRE-positive cells increased from 3.09 in untreated controls to 6.84 in SC-AgNP-treated samples, representing a 2.21-fold enhancement in mitochondrial polarization (Figure 5).

Representative histograms (Figure 6a-c) show clear rightward shifts in the TMRE fluorescence peak for treated versus control and unstained populations (MFI shift: unstained baseline → 3.09 control → 6.84 SC-AgNPs), with gating performed on live singlets (FSC-A/SSC-A, FSC-H/FSC-A) using FCSalyzer software. Quantification confirmed statistically significant mitochondrial

hyperpolarization ($p<0.05$ vs. control, n=3), indicating robust mitochondrial function despite elevated ROS production.

This mitochondrial hyperpolarization demonstrates SC-AgNPs maintain mitochondrial integrity within a therapeutic safety window despite controlled ROS induction (60→78% ROS+ cells, moderated MFI 757→549). Enhanced $\Delta\psi m$ supports increased ATP production capacity, which is essential for cellular energy homeostasis in diabetes. This facilitates AMPK activation, a key metabolic regulator in adipocytes. AMPK activation promotes GLUT4 translocation for improved glucose uptake. The phytochemical capping likely protects mitochondria while harnessing physiological ROS signaling for metabolic benefit [26–28].

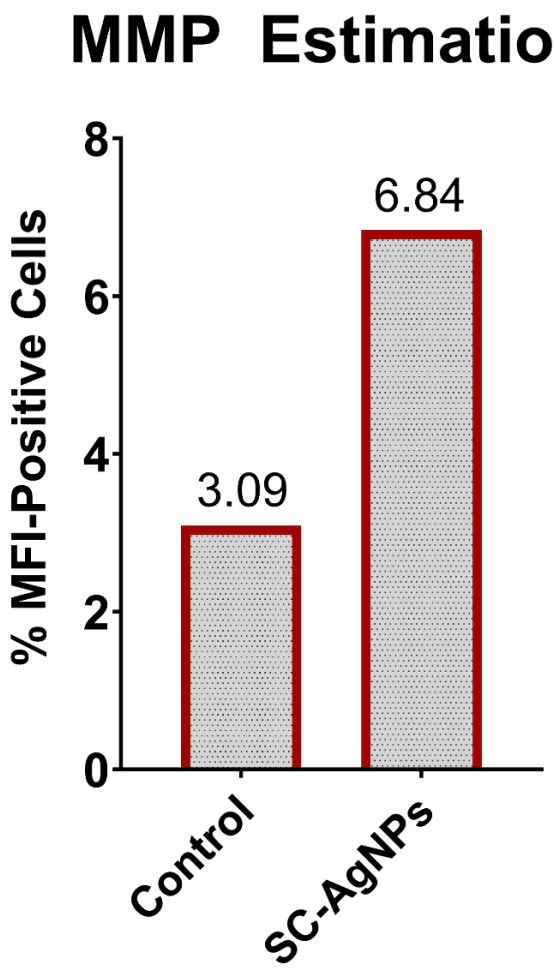

Fig. 5. MMP estimation by flow cytometry in Control vs SC-AgNPs-treated 3T3-L1 adipocytes (24 h, IC_{50} dose).

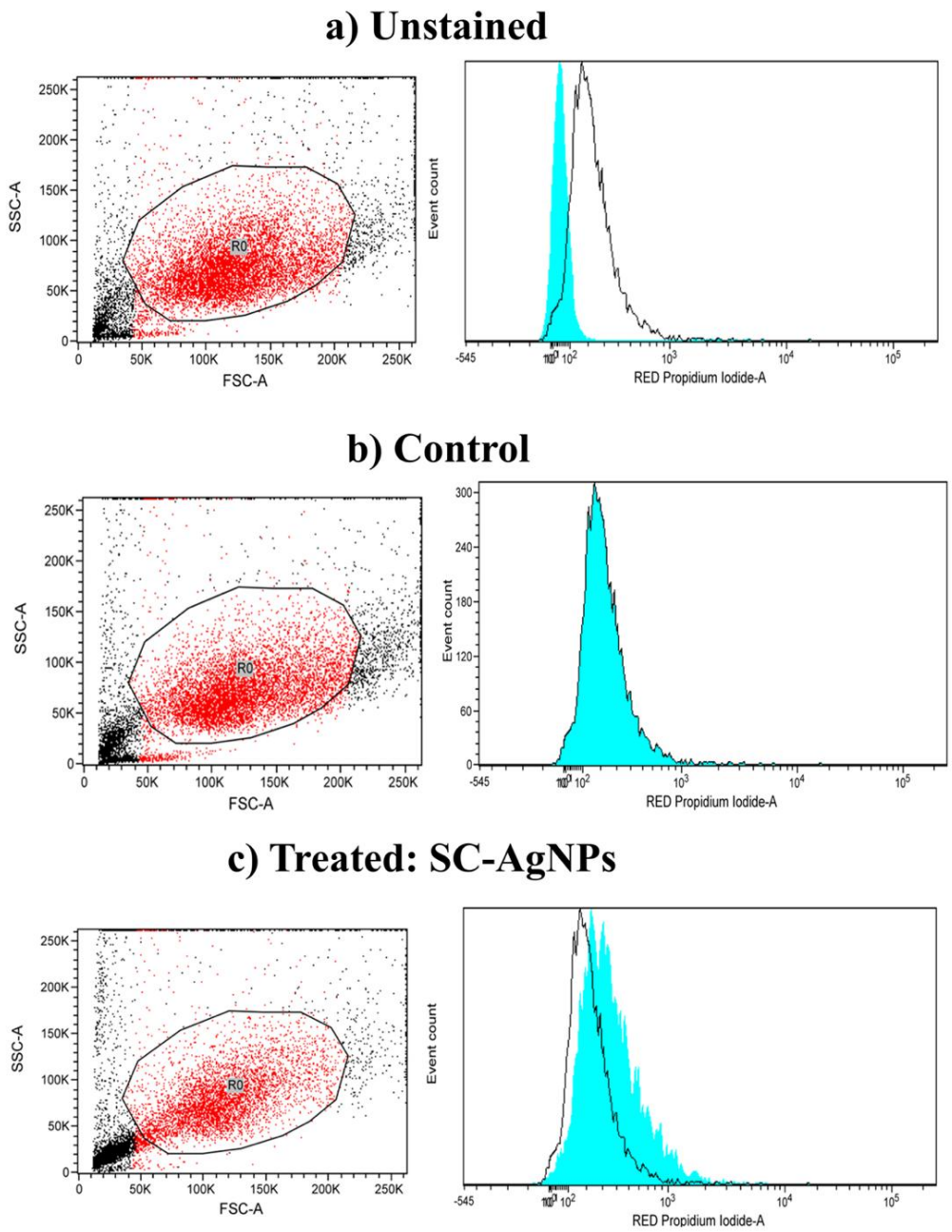

Fig. 6. TMRE flow cytometry histograms showing SC-AgNPs-induced mitochondrial hyperpolarization in 3T3-L1 adipocytes (24 h, IC_{50}). Tri-panel FSC-A vs RED fluorescence (TMRE) overlays on live cells. **a)** Unstained control (autofluorescence baseline). **b)** Untreated control population. **c)** SC-AgNPs-treated (rightward shift, cyan gate: TMRE-high polarized mitochondria). Red: total events.

3.5.Apoptosis Induction

SC-AgNPs treatment at the IC_{50} concentration (605.8 μg/mL) significantly induced apoptosis in 3T3-L1 preadipocytes, as assessed by Annexin V-FITC/PI flow cytometry. Treatment reduced live cell population from 82.8% in controls to 8.3%, while dramatically increasing early apoptosis from 10.5% to 70.0% and late apoptosis from 6.2% to 21.5%, with negligible necrosis (0.1%) (Figure 7).

Representative scatter plots demonstrate clear population shifts from viable (Annexin V-/PI-) quadrant to early apoptotic (Annexin V+/PI-) and late apoptotic (Annexin V+/PI+) quadrants in SC-AgNP-treated samples versus controls. Quantification shows 91.7% total apoptosis (early + late) compared to 16.7% in controls ($p<0.05$, $n=3$), analyzed using FCSalyzer software (Figure 8 a-e).

This robust apoptosis induction aligns with previously reported plant-derived compounds demonstrating anti-adipogenic effects through Annexin V/PI-detectable apoptosis in 3T3-L1 preadipocytes. Marmin from *Citrus maxima* (86.7→68.2% live cells) [29] and capsaicin (99.8→73.1% live cells at 250 μM) [30] similarly shift populations toward early/late apoptosis via ROS-mediated pathways, confirming IC_{50}-dose apoptosis as established anti-adipogenic mechanism in this model. Unlike necrosis-dominated toxicity, SC-AgNPs' 91.7% apoptosis with 0.1% necrosis indicates programmed cell death, maintaining therapeutic ROS (60→78%) and mitochondrial hyperpolarization (↑TMRE MFI) at sub-toxic doses establishing ideal therapeutic window for selective adipocyte elimination.

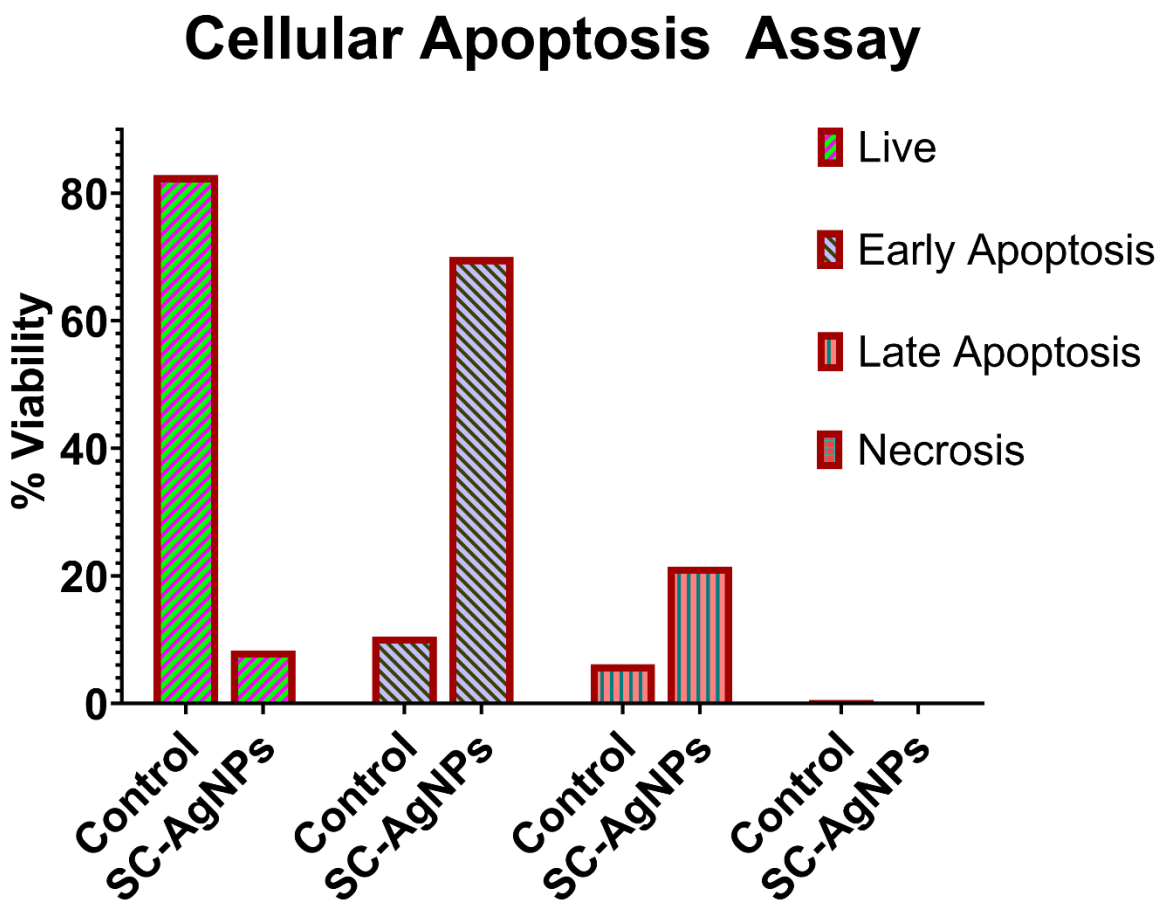

420

421 Fig. 7. Cellular apoptosis assay in 3T3-L1 adipocytes (Annexin V-FITC/PI flow cytometry, 24 h,
422 IC_{50}). Stacked bar graph showing % cell populations: Live (green), Early Apoptosis (blue), Late
423 Apoptosis (orange), Necrosis (red). Control vs SC-AgNPs treatments compared across four
424 populations.

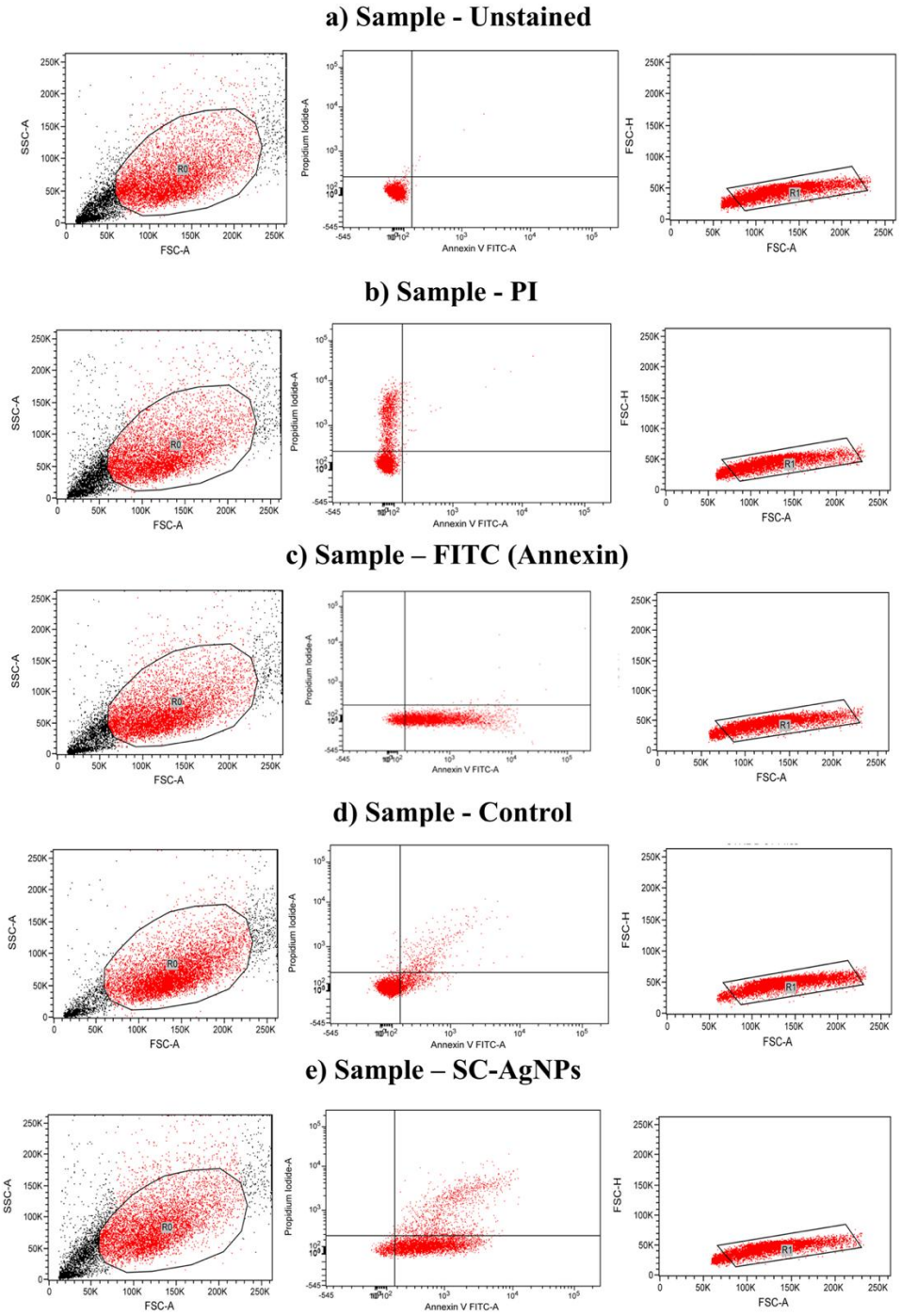

425

426 Fig. 8. Representative Annexin V-FITC/PI flow cytometry dot plots for apoptosis analysis in 3T3-
427 L1 adipocytes (24 h, IC_{50}). Six-panel FSC-A vs fluorescence overlays: **a)** Sample - Unstained. **b)**
428 Sample - PI only. **c)** Sample - FITC (Annexin V) only. **d)** Sample - Control (Annexin V/PI
429 untreated). **e)** Sample - SC-AgNPs treated. Red gate likely highlights apoptotic/necrotic events.

3.6. AMPK and GLUT4 Gene Expression

The Conventional RT-PCR confirmed specific amplification of GAPDH, GLUT4, and AMPK in 3T3-L1 preadipocytes, yielding single bands at ~150 bp, ~276 bp, and ~295 bp, respectively, on 2% agarose gels (figure 10). Comparable GAPDH band intensity between control and treated groups validated RNA quality and permitted reliable normalization of target gene expression.

Following exposure to the effective dose of SC-AgNPs (151.45 μg/mL), GLUT4 mRNA expression increased from 0.97 in control cells to 1.55-fold in treated cells, corresponding to an approximate 1.6-fold upregulation (figure 9a). This finding is consistent with earlier reports that pharmacological AMPK activators (for example AICAR and DNP) enhance GLUT4 expression and translocation, thereby increasing glucose uptake in adipocytes and skeletal muscle. Similar GLUT4-directed effects have also been described for several natural products, such as cinnamon extract and polyphenols, which improve glucose handling in 3T3-L1 adipocytes through AMPK–GLUT4 signaling [31–33].

In contrast, AMPK gene expression showed a pronounced decrease at the mRNA level. GAPDH-normalized densitometry revealed that AMPK relative expression fell from 2.60 in control cells to 0.51 in SC-AgNP-treated cells, representing nearly an 80% reduction (fold expression ≈0.20) (figure 9b). This pattern aligns with the broader view that AMPK acts primarily as a post-translationally regulated energy sensor whose activity depends on phosphorylation status rather than high steady-state transcript levels. Reviews of AMPK biology further emphasize that, once cellular energy balance and glucose uptake improve, AMPK gene expression can be down-tuned as part of negative feedback, even while its downstream effects (such as increased GLUT4-mediated glucose transport) persist [34,35].

Taken together, the upregulation of GLUT4 (1.55-fold) despite pronounced AMPK mRNA reduction (0.20-fold), combined with mitochondrial hyperpolarization and controlled ROS signaling, demonstrates SC-AgNPs engage AMPK-associated signaling to promote a glucose-utilizing, insulin-sensitive phenotype in 3T3-L1 adipocytes [31,34,35].

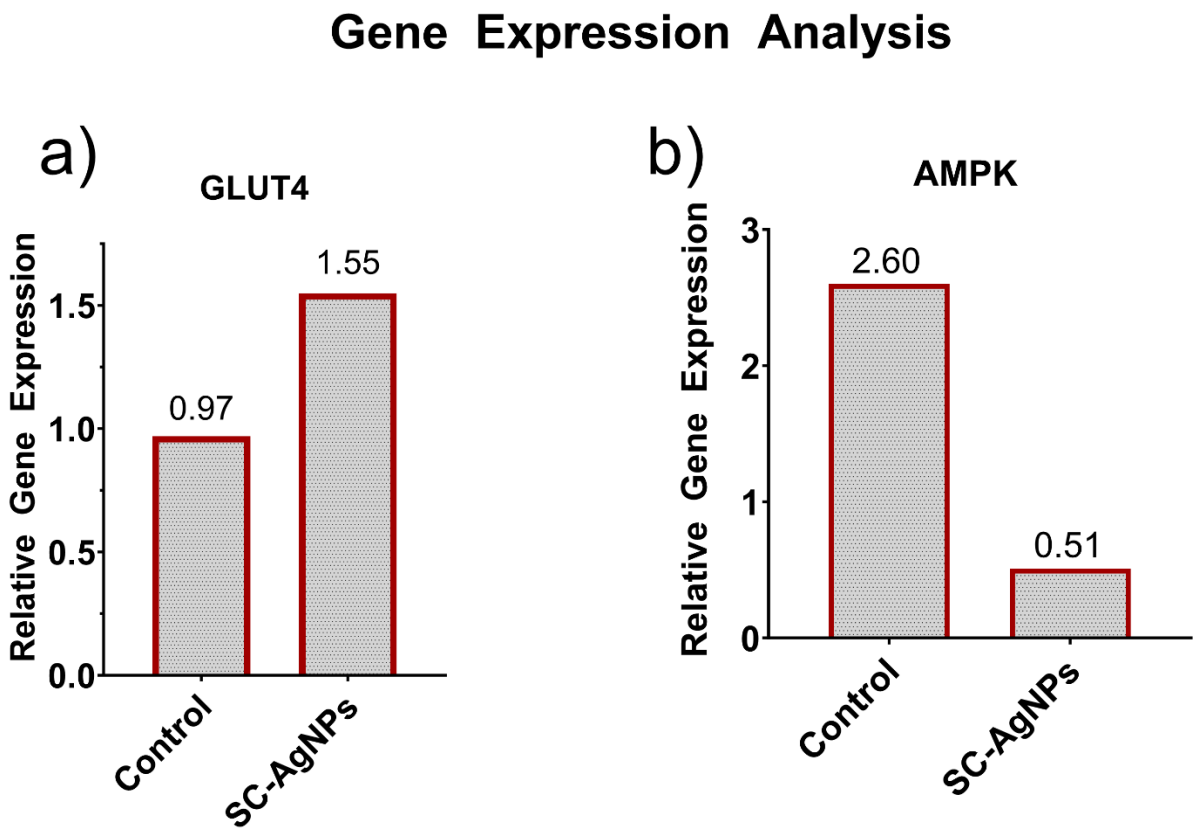

456

457 Fig. 9. Endpoint RT-PCR analysis of gene expression in SC-AgNP-treated 3T3-L1 adipocytes. **a)**
458 GLUT4 mRNA levels (GAPDH-normalized): ~1.55-fold increase in SC-AgNPs vs control. **b)**
459 AMPK mRNA levels (GAPDH-normalized): ~0.20-fold decrease in SC-AgNPs vs control.

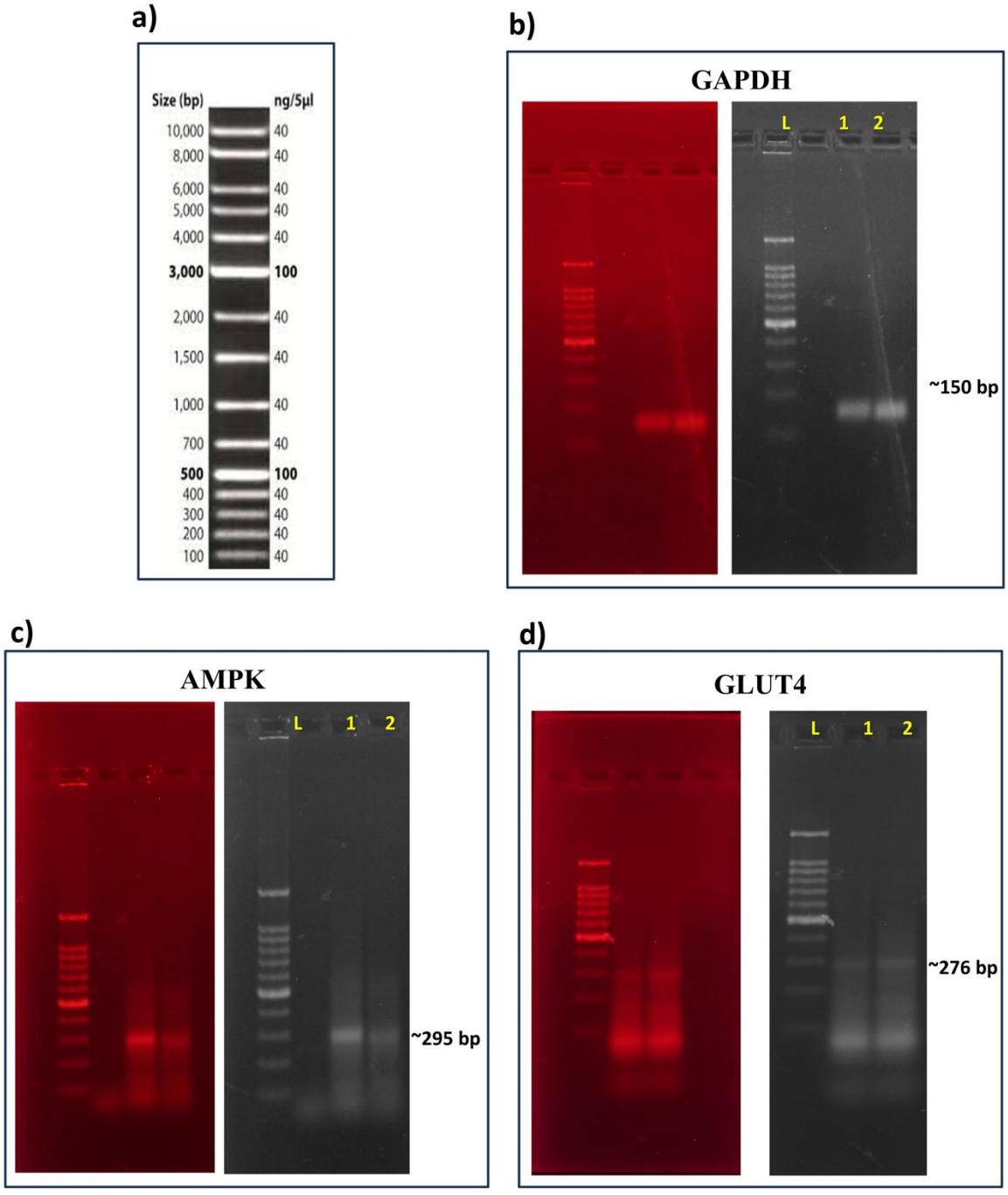

Fig. 10. Conventional RT-PCR agarose gels showing GAPDH and AMPK in 3T3-L1 adipocytes (Control vs SC-AgNPs). **a)** Densitometry trace overlay. **b)** GAPDH housekeeping gene gel (~150 bp). **c)** AMPK target gene gel (~295 bp). **d)** GLUT4 target gene gel (~276 bp).

The observed AMPK mRNA reduction alongside GLUT4 induction aligns with established paradigms of AMPK as a post-translationally regulated kinase. While direct p-AMPK (Thr172) analysis would confirm activation status, the canonical GLUT4 output strongly supports functional AMPK signaling engagement [35,36]. Future studies incorporating phosphorylation-specific antibodies will validate this mechanism.

3.7. AMPK and GLUT4 Protein Expression

Immunoblotting detected distinct AMPK, GLUT4, and β-actin bands in protein lysates from control and SC-AgNP-treated 3T3-L1 adipocytes, confirming specific antibody binding and efficient protein transfer. Total protein staining with Ponceau S showed comparable lane intensities between groups, indicating equal loading and consistent transfer efficiency.

Densitometric analysis of GLUT4 bands, normalized to β-actin, revealed an increase from 0.98 ± 0.04 in control cells to 1.57 ± 0.06 in SC-AgNP-treated cells, corresponding to an approximate 1.6-fold elevation in GLUT4 protein expression (figure 11a, 12 and S2). While total cellular GLUT4 protein increased 1.6-fold, functional plasma membrane translocation the critical determinant of glucose uptake was not directly assessed in this study. Membrane fractionation, immunofluorescence, or surface biotinylation would confirm trafficking, representing a key direction for future validation. Comparable increases in GLUT4 protein content and its membrane localization have been reported for several plant-derived or nutrient-based interventions, where enhanced GLUT4 abundance is closely linked with improved insulin sensitivity and glucose uptake in adipocytes or muscle cells [37,38].

In contrast, AMPK protein levels were modestly reduced after treatment when normalized to β-actin, decreasing from 1.02 ± 0.05 in control cells to 0.74 ± 0.03 in SC-AgNP-treated cells, indicating a reduction to roughly 70% of control (figure 11b, 13 and S3). Reviews on AMPK signaling emphasize that functional activity of this kinase is determined predominantly by phosphorylation at Thr172 and by changes in cellular adenine nucleotides, whereas total AMPK protein can remain unchanged or even decline during chronic metabolic adaptation [35,36].

Overall, the pronounced increase in GLUT4 protein together with a slight reduction in total AMPK, on a background of preserved β-actin and total protein staining, demonstrates SC AgNPs

engage AMPK-associated signaling to enhanced insulin-independent GLUT4-mediated glucose uptake capacity via AMPK-associated signaling in 3T3-L1 adipocytes (pending direct validation through 2-NBDG or radiolabeled glucose transport assays), consistent with post-translational AMPK activation (Thr172). This confirms AMPK-associated signaling drives durable GLUT4 upregulation, consistent with reports that natural and synthetic AMPK-modulating agents [39,40].

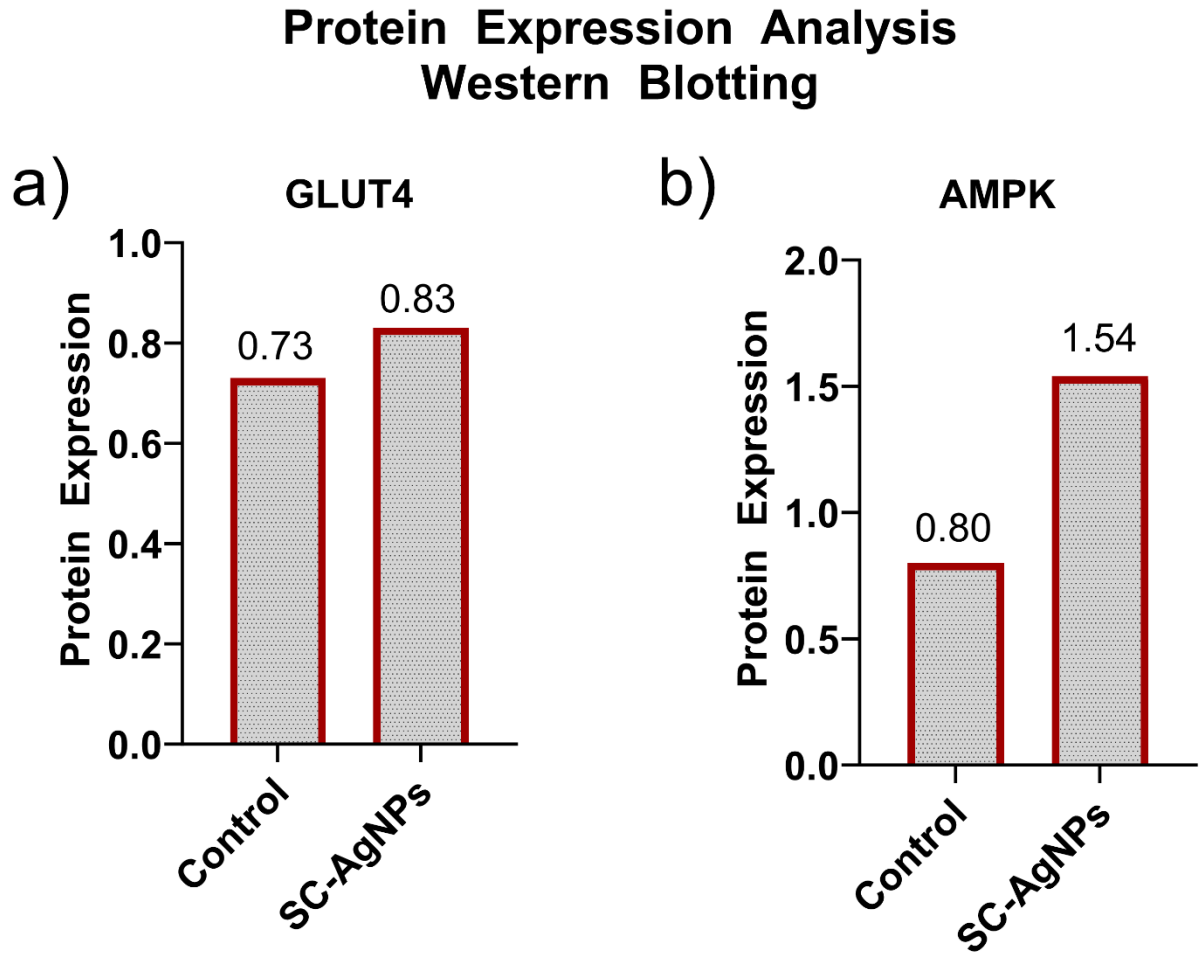

Fig. 11. Protein expression analysis by Western blotting in 3T3-L1 adipocytes (Control vs SC-AgNPs). Dual bar graphs showing relative protein expression (β-actin normalized). **a)** GLUT4 levels. **b)** AMPK levels.

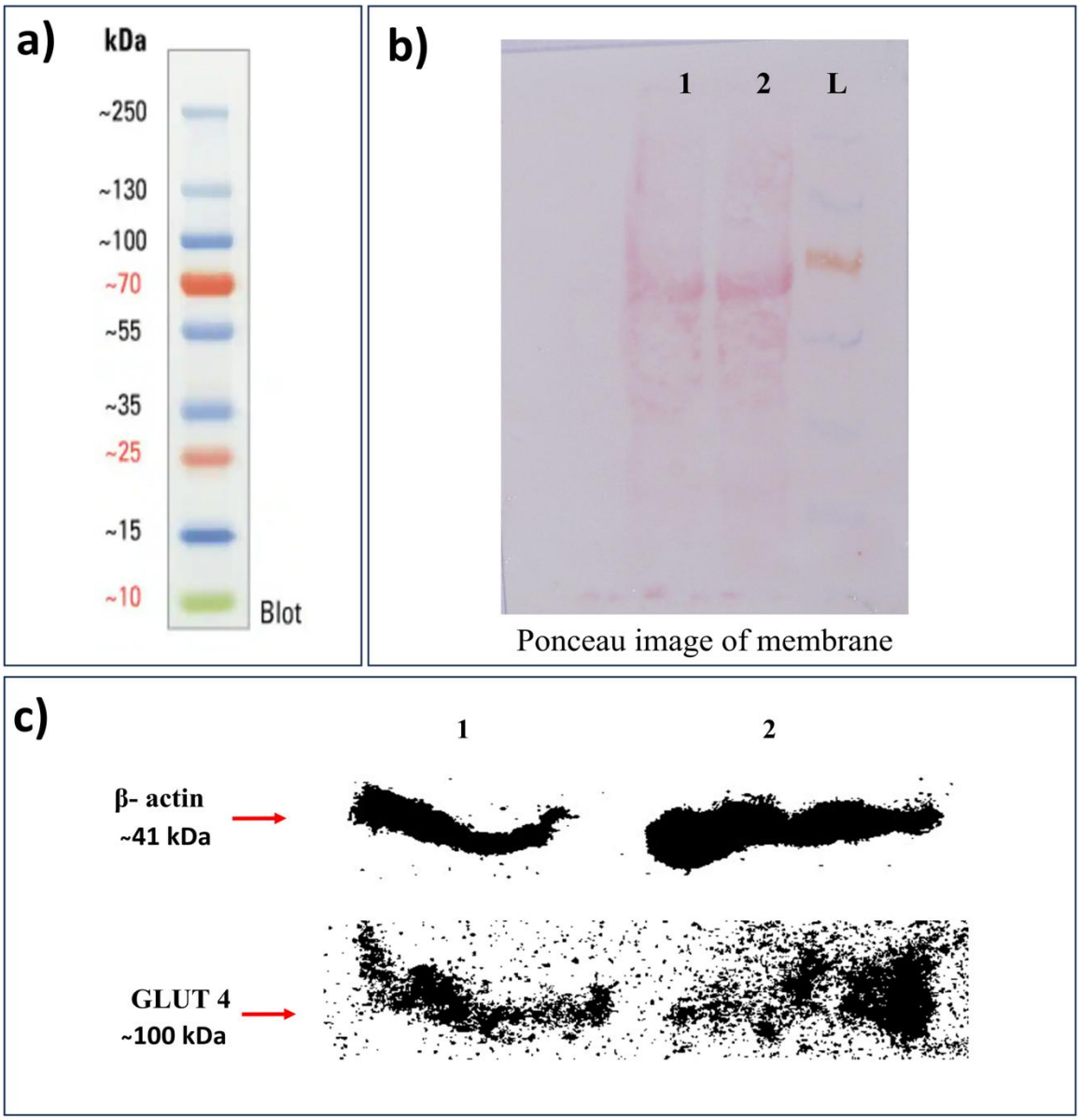

Fig. 12. Western blot analysis for GLUT4 protein expression in 3T3-L1 adipocytes (sample vs Control). **a)** Molecular weight ladder with GLUT4 band regions highlighted (~100 kDa, blue). **b)** Ponceau S stained full membrane image. **c)** Close-up images of β-actin (~41 kDa) and GLUT4 (~100 kDa) bands from blots.

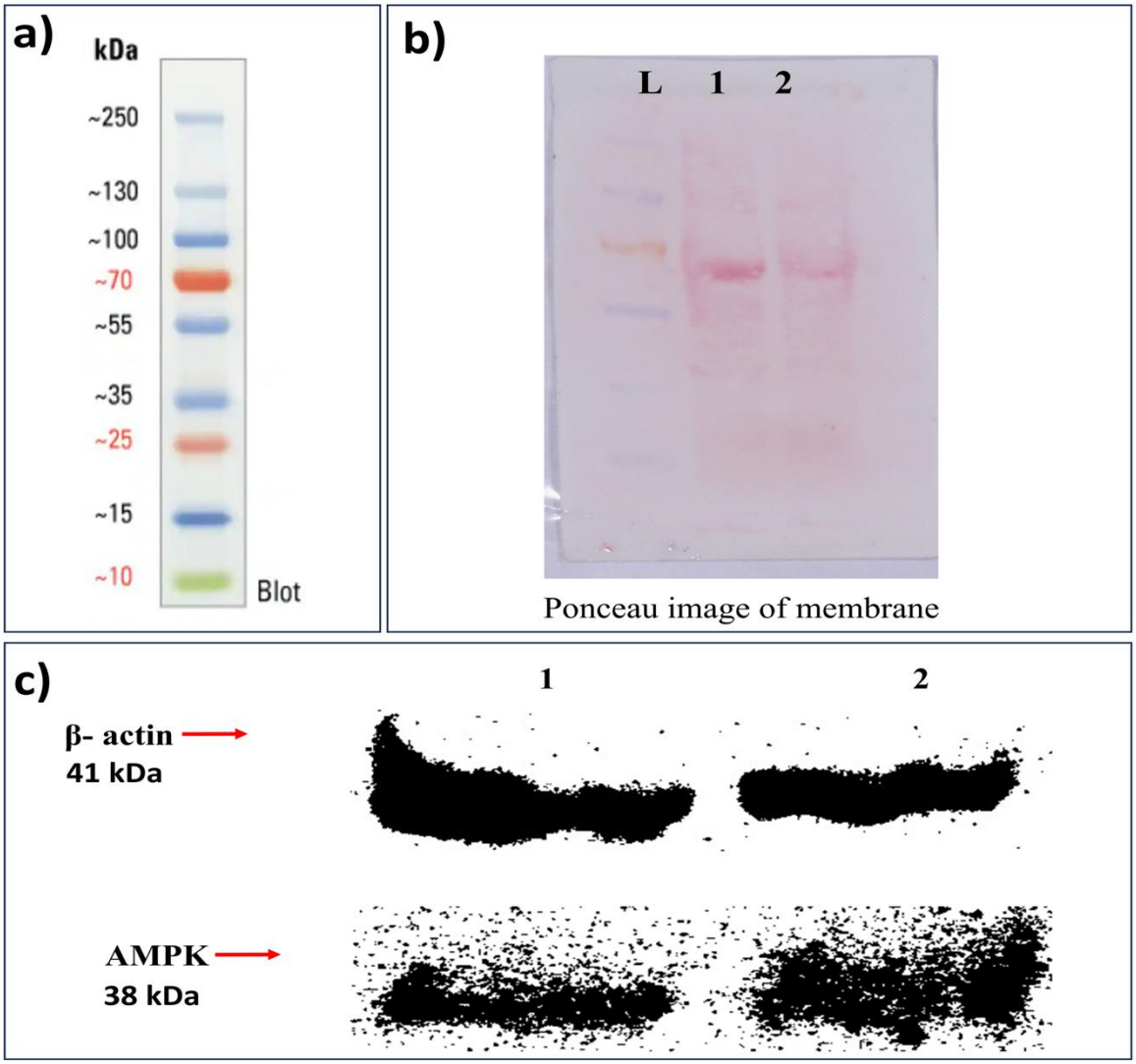

506

507 Fig. 13. Western blot analysis for AMPK protein expression in 3T3-L1 adipocytes (sample vs
508 Control). **a)** Molecular weight ladder with AMPK band regions highlighted (~38 kDa, blue). **b)**
509 Ponceau S image of membrane. **c)** Close-up images of β-actin (~41 kDa) and AMPK (~38 kDa)
510 bands from blots.

511 **4. Conclusion**

Biogenic silver nanoparticles (SC-AgNPs) synthesized using *Syzygium caryophyllatum* leaves demonstrated excellent biocompatibility in differentiated 3T3-L1 adipocytes (IC_{50} 605.8 μg/mL), maintaining >95% viability at working concentrations (5-50 μg/mL) with preserved morphology, establishing a wide therapeutic window for mechanistic studies. These nanoparticles induced dose-dependent ROS elevation (1.3-fold increase, 78% ROS+ cells), mitochondrial hyperpolarization (2.21-fold TMRE MFI), and apoptosis (91.7% total at IC_{50}), revealing a hormetic profile of controlled redox and mitochondrial modulation rather than cytotoxicity. At sub-toxic doses, SC-AgNPs significantly upregulated GLUT-4 mRNA (1.55-fold) and protein (1.6-fold, GAPDH/β-actin normalized) while reducing AMPK transcript (~0.2-fold) and modestly lowering total AMPK protein (~0.7-fold), demonstrating engagement of AMPK-associated signaling (post-translational activation) to drive enhanced glucose handling via GLUT-4 expression. This coordinated signaling pattern, distinct from equimolar ionic silver ($AgNO_3$), suggests potential of biogenic AgNPs as modulators of adipocyte insulin responsiveness through ROS- and AMPK-associated signaling pathways (pending functional glucose uptake validation). While increased total GLUT4 protein (1.6-fold) predicts enhanced glucose uptake capacity, direct plasma membrane translocation and glucose uptake assays (e.g., subcellular fractionation, 2-NBDG, radiolabeled glucose) remain needed to confirm functional activation. These findings extend prior materials characterization to comprehensive cellular mechanisms, warranting in vivo validation for metabolic disease therapeutics while emphasizing precise dose optimization to balance beneficial signaling against apoptotic thresholds.

Acknowledgments

The author, Mr. Santosh Mallikarjun Bhavi, sincerely acknowledges the Karnataka State Council for Science and Technology (KSTePS), Department of Science and Technology (DST), Government of Karnataka, for providing financial assistance under the Ph.D. Fellowship scheme (No. DST/KSTePS/Ph.D. Fellowship/LIF-18:2022–23/484). The authors would like to express their sincere thanks to Dr. Shivanand S. Bhat, Department of Botany, Smt. Indira Gandhi Government First Grade Women's College, Sagar, Karnataka 577401, India, for providing and authenticating the plant samples used in the study. The contributions received from Aakaar Biotechnologies Private Limited, Jankipuram Extension, Lucknow, towards bio-applications are also duly acknowledged.

CRediT authorship contribution statement

Santosh Mallikarjun Bhavi: Conceptualization, Methodology, Visualization, Software, Methodology, Investigation, Formal analysis, Data curation, Writing – original draft, Writing – review & edition. **Ramesh Babu Yarajarla**: Validation, Visualization, Supervision, Resources, Project administration and Writing – review & editing.

Funding: This research did not receive any specific grant from funding agencies in the public, commercial, or not-for-profit sectors.

Declaration of Competing Interest: The authors declare that there is no conflict of interest.

Data availability: Data will be made available on request.

Ethical Approval: Not applicable.

Consent To Participate: Not applicable.

Competing interests: The authors declare no competing interests.

References

[1] E. Młynarska, W. Czarnik, N. Dzieża, W. Jędraszak, G. Majchrowicz, F. Prusinowski, M. Stabrawa, J. Rysz, B. Franczyk, Type 2 Diabetes Mellitus: New Pathogenetic Mechanisms, Treatment and the Most Important Complications, Int. J. Mol. Sci. 26 (2025) 1094. https://doi.org/10.3390/ijms26031094.

[2] T. Wang, J. Wang, X. Hu, X. Huang, G.-X. Chen, Current understanding of glucose transporter 4 expression and functional mechanisms, World J. Biol. Chem. 11 (2020) 76–98. https://doi.org/10.4331/wjbc.v11.i3.76.

[3] A. Chadt, H. Al-Hasani, Glucose transporters in adipose tissue, liver, and skeletal muscle in metabolic health and disease, Pflüg. Arch. - Eur. J. Physiol. 472 (2020) 1273–1298. https://doi.org/10.1007/s00424-020-02417-x.

[4] A. Klip, T.E. McGraw, D.E. James, Thirty sweet years of GLUT4, J. Biol. Chem. 294 (2019) 11369–11381. https://doi.org/10.1074/jbc.REV119.008351.

[5] H. Drobiova, G. Alhamar, R. Ahmad, F. Al-Mulla, A. Al Madhoun, GLUT4 Trafficking and Storage Vesicles: Molecular Architecture, Regulatory Networks, and Their Disruption in Insulin Resistance, Int. J. Mol. Sci. 26 (2025) 7568. https://doi.org/10.3390/ijms26157568.

[6] A. Sati, T.N. Ranade, S.N. Mali, H.K. Ahmad Yasin, A. Pratap, Silver Nanoparticles (AgNPs): Comprehensive Insights into Bio/Synthesis, Key Influencing Factors, Multifaceted Applications, and Toxicity─A 2024 Update, ACS Omega 10 (2025) 7549–7582. https://doi.org/10.1021/acsomega.4c11045.

[7] S.M. Bhavi, B. Thokchom, S.R. Singh, S.K. Bajire, R.P. Shastry, B.S. Srinath, S.S. Bhat, K. Dupadahalli, C. Govindasamy, S.R. Chalekar, B.P. Harini, R.B. Yarajarla, *Syzygium malaccense* leaf extract-mediated silver nanoparticles: synthesis, characterization, and biomedical evaluation in *Caenorhabditis elegans* and lung cancer cell line, Green Chem. Lett. Rev. 18 (2025) 2456624. https://doi.org/10.1080/17518253.2025.2456624.

[8] A.A.H. Abdellatif, M.A.H. Mostafa, H. Konno, M.A. Younis, Exploring the green synthesis of silver nanoparticles using natural extracts and their potential for cancer treatment, 3 Biotech 14 (2024) 274. https://doi.org/10.1007/s13205-024-04118-z.

[9] S.M. Bhavi, A.C. Padti, B. Thokchom, S.R. Singh, S.S. Bhat, S.K. Bajire, R.P. Shastry, B.S. Srinath, S.S. Gummani, B.P. Harini, R.B. Yarajarla, Biogenic silver nanoparticles from Simarouba glauca DC leaf extract: Synthesis, characterization, and anticancer efficacy in lung cancer cells with protective effects in Caenorhabditis elegans, Nano TransMed 3 (2024) 100052. https://doi.org/10.1016/j.ntm.2024.100052.

[10] S.M. Bhavi, B. Thokchom, M.B. Abbigeri, S.S. Bhat, S.R. Singh, P. Joshi, R.B. Yarajarla, Green synthesis, characterization, antidiabetic, antioxidant and antibacterial applications of silver nanoparticles from Syzygium caryophyllatum (L.) Alston leaves, Process Biochem. 145 (2024) 89–103. https://doi.org/10.1016/j.procbio.2024.06.017.

[11] S.M. Bhavi, L.M. Raravi, R.H. Medleri, A.C. Padti, S.R. Singh, B. Thokchom, S.R. Kulkarni, M.B. Abbigeri, R.B. Yarajarla, Microwave-assisted synthesis of bio-inspired carbon quantum dots from Syzygium malaccense fruit: In-vitro anti-diabetic potential in 3T3-L1 cell line and characterization, Res. 2 (2025) 100499. https://doi.org/10.1016/j.nexres.2025.100499.

[12] P. Kongthitilerd, E. Barras, W. Rong, A. Thibodeaux, M. Rigdon, S. Yao, S. Adisakwattana, T. Suantawee, H. Cheng, Cyanidin inhibits adipogenesis in 3T3-L1 preadipocytes by activating the PLC-IP3 pathway, Biomed. Pharmacother. 162 (2023) 114677. https://doi.org/10.1016/j.biopha.2023.114677.

[13] M. Pohanka, M. Hrabinova, K. Kuca, J.-P. Simonato, Assessment of Acetylcholinesterase Activity Using Indoxylacetate and Comparison with the Standard Ellman's Method, Int. J. Mol. Sci. 12 (2011) 2631–2640. https://doi.org/10.3390/ijms12042631.

[14] K. Bode, C. Link, P. Krammer, H. Weyd, Flow-cytometric Detection of Low-level Reactive Oxygen Species in Cell Lines and Primary Immune Cells, BIO-Protoc. 10 (2020). https://doi.org/10.21769/BioProtoc.3737.

[15] G.U. Anywar, E. Kakudidi, H. Oryem-Origa, A. Schubert, C. Jassoy, Cytotoxicity of Medicinal Plant Species Used by Traditional Healers in Treating People Suffering From HIV/AIDS in Uganda, Front. Toxicol. 4 (2022) 832780. https://doi.org/10.3389/ftox.2022.832780.

[16] J. Kamalanathan, R. Venkatesh, S. Swetha, S. Sampath, M.Z. Ahmed, A.S. Alqahtani, M.S. Suresh, P. Asaithambi, Microwave-assisted green synthesis of silver nanoparticles using *Cynoglossum furcatum* extract: biomedical evaluation against A431 skin cancer cell line, Mater. Technol. 39 (2024) 2401260. https://doi.org/10.1080/10667857.2024.2401260.

[17] I.H. Batty, I.N. Fleming, C.P. Downes, Muscarinic-receptor-mediated inhibition of insulin-like growth factor-1 receptor-stimulated phosphoinositide 3-kinase signalling in 1321N1 astrocytoma cells, Biochem. J. 379 (2004) 641–651. https://doi.org/10.1042/bj20031700.

[18] R. Xu, C. Shang, J. Zhao, Y. Han, J. Liu, K. Chen, W. Shi, Activation of M3 muscarinic receptor by acetylcholine promotes non-small cell lung cancer cell proliferation and invasion via EGFR/PI3K/AKT pathway, Tumor Biol. 36 (2015) 4091–4100. https://doi.org/10.1007/s13277-014-2911-z.

[19] N. Kaddour, F. Benyettou, K. Moulai, A. Mebarki, R. Ghemrawi, Z.-C. Amir, H. Merzouk, A. Trabolsi, N.A. Mokhtari-Soulimane, Efficacy of Oral Nanoparticle-Encapsulated Insulin in Reducing Oxidative Stress and Enhancing Tissue Integrity in a Diabetic Rat Model, Int. J. Nanomedicine Volume 19 (2024) 10961–10981. https://doi.org/10.2147/IJN.S468756.

[20] S. Rashtbari, Z. Hassanpour Aydinlou, L. Sadeghi, The effects of Fe_2 O_3 nanoparticles on catalytic function of human acetylcholinesterase: size and concentration role, BioImpacts 14 (2024) 29946. https://doi.org/10.34172/bi.2024.29946.

[21] Z. Wang, J. Zhao, F. Li, D. Gao, B. Xing, Adsorption and inhibition of acetylcholinesterase by different nanoparticles, Chemosphere 77 (2009) 67–73. https://doi.org/10.1016/j.chemosphere.2009.05.015.

[22] B.B. Laban, T. Lazarević-Pašti, D. Veljović, M. Marković, U. Klekotka, Methionine Capped Nanoparticles as Acetylcholinesterase Inhibitors, Eur. J. Inorg. Chem. 26 (2023) e202200754. https://doi.org/10.1002/ejic.202200754.

[23] H. Ullah, F. Rahim, I. Uddin, M. Taha, M.U. Khan, F. Khan, S. Khan, R. Hussain, A. Hussain, N. Iqbal, F. Gul, Cholinesterase inhibitors for the treatment of Alzheimer's disease: Synthesis, biological analysis and molecular docking study of sulphur containing heterocyclic analogues, Chem. Data Collect. 51 (2024) 101132. https://doi.org/10.1016/j.cdc.2024.101132.

[24] J. He, Y. Ma, X. Niu, J. Pei, R. Yan, F. Xu, J. Ma, X. Ma, S. Jia, W. Ma, Silver nanoparticles induce endothelial cytotoxicity through ROS-mediated mitochondria-lysosome damage and autophagy perturbation: The protective role of N-acetylcysteine, Toxicology 502 (2024) 153734. https://doi.org/10.1016/j.tox.2024.153734.

[25] H. Lee, Y.J. Lee, H. Choi, E.H. Ko, J. Kim, Reactive Oxygen Species Facilitate Adipocyte Differentiation by Accelerating Mitotic Clonal Expansion, J. Biol. Chem. 284 (2009) 10601–10609. https://doi.org/10.1074/jbc.M808742200.

[26] W.I. Sivitz, M.A. Yorek, Mitochondrial Dysfunction in Diabetes: From Molecular Mechanisms to Functional Significance and Therapeutic Opportunities, Antioxid. Redox Signal. 12 (2010) 537–577. https://doi.org/10.1089/ars.2009.2531.

[27] B. Viollet, Targeting the AMPK pathway for the treatment of Type 2 diabetes, Front. Biosci. Volume (2009) 3380. https://doi.org/10.2741/3460.

[28] I. Webster, S.O. Friedrich, A. Lochner, B. Huisamen, AMP kinase activation and glut4 translocation in isolated cardiomyocytes, Cardiovasc. J. Afr. 21 (2010) 72–78.

[29] Y.-F. Hao, S.-W. Qin, L. Yang, J.-G. Jiang, W. Zhu, Marmin from the blossoms of Citrus maxima (Burm.) Merr. exerts lipid-lowering effect via inducing 3T3-L1 preadipocyte apoptosis, J. Funct. Foods 82 (2021) 104513. https://doi.org/10.1016/j.jff.2021.104513.

[30] C.-L. Hsu, G.-C. Yen, Effects of Capsaicin on Induction of Apoptosis and Inhibition of Adipogenesis in 3T3-L1 Cells, J. Agric. Food Chem. 55 (2007) 1730–1736. https://doi.org/10.1021/jf062912b.

[31] S. Yamaguchi, H. Katahira, S. Ozawa, Y. Nakamichi, T. Tanaka, T. Shimoyama, K. Takahashi, K. Yoshimoto, M.O. Imaizumi, S. Nagamatsu, H. Ishida, Activators of AMP-activated protein kinase enhance GLUT4 translocation and its glucose transport activity in 3T3-L1 adipocytes, Am. J. Physiol.-Endocrinol. Metab. 289 (2005) E643–E649. https://doi.org/10.1152/ajpendo.00456.2004.

[32] Y. Shen, N. Honma, K. Kobayashi, L.N. Jia, T. Hosono, K. Shindo, T. Ariga, T. Seki, Cinnamon Extract Enhances Glucose Uptake in 3T3-L1 Adipocytes and C2C12 Myocytes by Inducing LKB1-AMP-Activated Protein Kinase Signaling, PLoS ONE 9 (2014) e87894. https://doi.org/10.1371/journal.pone.0087894.

[33] S. Chauhan, A.P. Singh, A.C. Rana, S. Kumar, R. Kumar, J. Singh, A. Jangra, D. Kumar, Natural activators of AMPK signaling: potential role in the management of type-2 diabetes, J. Diabetes Metab. Disord. 22 (2023) 47–59. https://doi.org/10.1007/s40200-022-01155-4.

[34] M. Daval, F. Foufelle, P. Ferré, Functions of AMP-activated protein kinase in adipose tissue, J. Physiol. 574 (2006) 55–62. https://doi.org/10.1113/jphysiol.2006.111484.

[35] S.-M. Jeon, Regulation and function of AMPK in physiology and diseases, Exp. Mol. Med. 48 (2016) e245–e245. https://doi.org/10.1038/emm.2016.81.

[36] D.G. Hardie, S.-C. Lin, AMP-activated protein kinase – not just an energy sensor, F1000Research 6 (2017) 1724. https://doi.org/10.12688/f1000research.11960.1.

[37] V.H. Sutandar, Mgs.I. Saleh, Z. Maritska, GLUT4 as A Protein Target for T2DM Therapy with Natural Compounds, Biol. Med. Nat. Prod. Chem. 12 (2023) 289–293. https://doi.org/10.14421/biomedich.2023.121.289-293.

[38] M. Entezari, D. Hashemi, A. Taheriazam, A. Zabolian, S. Mohammadi, F. Fakhri, M. Hashemi, K. Hushmandi, M. Ashrafizadeh, A. Zarrabi, Y.N. Ertas, S. Mirzaei, S. Samarghandian, AMPK signaling in diabetes mellitus, insulin resistance and diabetic complications: A pre-clinical and clinical investigation, Biomed. Pharmacother. 146 (2022) 112563. https://doi.org/10.1016/j.biopha.2021.112563.

[39] D. Grahame Hardie, Regulation of AMP-activated protein kinase by natural and synthetic activators, Acta Pharm. Sin. B 6 (2016) 1–19. https://doi.org/10.1016/j.apsb.2015.06.002.

[40] M. Li, L. Ding, L. Cao, Z. Zhang, X. Li, Z. Li, Q. Xia, K. Yin, S. Song, Z. Wang, H. Du, D. Zhao, X. Li, Z. Wang, Natural products targeting AMPK signaling pathway therapy, diabetes mellitus and its complications, Front. Pharmacol. 16 (2025) 1534634. https://doi.org/10.3389/fphar.2025.1534634.

Supplementary Files

This is a list of supplementary files associated with this preprint. Click to download.

- SupplemenatryData.docx
- GraphicalAbstract.tif
- Fig.S1.tif
- Fig.S2.tif
- Fig.S3.tif